https://doi.org/10.5194/angeo-2020-39
Preprint. Discussion started: 23 June 2020

Annales Geophysicae Discussions

Analyses of different propagation models for the estimation of the topside ionosphere and plasmasphere with an Ensemble Kalman Filter

Tatjana Gerzen[1], David Minkwitz[2], Michael Schmidt[1], Eren Erdogan[1]
[1] Technical University Munich (TUM), Deutsches Geodätisches Forschungsinstitut (DGFI), Arcisstr. 21, Munich, Germany
[2] Airbus Defence and Space, Robert-Koch-Str. 1, Taufkirchen, Germany

Correspondence to: Tatjana Gerzen (tatjana.gerzen@tum.de)

Abstract.

The accuracy and availability of satellite-based applications like GNSS positioning and remote sensing crucially depends on the knowledge of the ionospheric electron density distribution. The tomography of the ionosphere is one of the major tools to provide link specific ionospheric corrections as well as to study and monitor physical processes in the ionosphere and plasmasphere. In this work, we apply an Ensemble Kalman Filter (EnKF) approach for the 4D electron density reconstruction of the topside ionosphere and plasmasphere with the focus on the investigation of different propagation models and compare them with the iterative reconstruction technique SMART+. The STEC measurements of eleven LEO satellites are assimilated into the reconstructions. We conduct a case study on a global grid with altitudes between 430 and 20200 km, for two periods of the year 2015 covering quiet to perturbed ionospheric conditions. Particularly, the performance of the methods to estimate independent STEC and electron density measurements from the three Swarm satellites is analysed. The results indicate that the methods EnKF with Exponential decay as the propagation model and SMART+ perform best, providing in summary the lowest residuals.

1 Introduction

The ionosphere is the upper part of the atmosphere extending from about 50 - 1000 km and going over in the plasmasphere. The characteristic property of the ionosphere is that it contains sufficient free electrons to affect the radio waves propagation of trans-ionospheric radio signals, as from telecommunication, navigation or remote sensing satellites, by refraction, diffraction and scattering.

Therefore, the knowledge of the three-dimensional electron density distribution and their dynamics are of practical importance. Around 50% of the signal delays or range errors of L-band signals used in GNSS originate from altitudes above the ionospheric F2 layer, which consist of topside ionosphere going over into the plasmasphere. So far, especially the topside ionosphere and plasmasphere is not well described.

The choice of the ionospheric correction model has an essential impact on the accuracy of the estimated ionospheric delay and its uncertainties. A widely used approach for ionospheric modelling is the single-layer model, whereby the ionosphere is projected onto a two-dimensional (2D) spherical layer, typically located between 350 and 450 km. However, usually 2D models are not accurate enough to support high accuracy navigation and positioning techniques in real time (e.g. Odijk 2002; Banville 2014). Additionally, they do not provide the possibility to look insight the complex coupling processes between magnetosphere, plasmasphere and ionosphere. More accurate and precise positioning is achievable by considering the ionosphere as 3D medium. There are several activities in the ionosphere community aiming to describe the median ionospheric behavior by the

https://doi.org/10.5194/angeo-2020-39
Preprint. Discussion started: 23 June 2020

Annales Geophysicae Discussions

development of 3D electron density models based on long-term historical data. Two widely used models are the International Reference Ionosphere model (IRI, cf. Bilitza et al., 2011) and the NeQuick model (cf. Nava et al., 2008).

Since those models represent a median behavior, it is essential to update them by the assimilation of actual ionospheric measurements. There is a variety of approaches developed and validated for the ionospheric reconstruction by combination of actual observations with an empirical or a physical background model. Hernandez-Pajares et al. (1999) present one of the first GNSS-based data-driven tomographic models which considers the ionosphere as a grid of three-dimensional voxels and the electron density within each voxel is computed as a random walk time series. The voxel-based discretisation of the ionosphere is used for instance in Heise et al., 2002; Wen et al., 2007; Gerzen and Minkwitz, 2016, Gerzen et al., 2017, Wen et al., 2020. These authors reconstruct the 3D ionosphere by algebraic iterative methods. An alternative is to estimate the electron density as a linear combination of smooth and continuous basis functions, like e.g. spherical harmonics (SPH) (Schaer 1999), B-splines (Schmidt et al., 2008; Zeilhofer, 2008; Zeilhofer et al., 2010; Olivares-Pulido et al., 2019), B-splines and trigonometric B-splines (Schmidt et al. 2015), B-splines and Chapman functions (Liang et al., 2015 and 2016), and empirical orthogonal functions and spherical harmonics (Howe et al., 1998).

Besides the algebraic methods, also techniques taking benefit of information on spatial and temporal covariance information, such as Optimal Interpolation, Kalman Filter, three- and four-dimensional variational techniques and Kriging, are applied to update the modelled electron density distributions, cf. Howe et al., 1998; Angling et al., 2008; Minkwitz et al., 2015 and 2016; Nikoukar et al., 2015; Olivares-Pulido et al., 2019.

Moreover, there are approaches based on physical models, which combine the estimation of the electron density with physical related variables such as neutral winds or the oxygen/nitrogen ratio (cf. Wang, et al. 2004; Scherliess et al., 2009; Lee et al., 2012; Lomidze et al., 2015; Schunk, et al., 2004 and 2016; Elvidge and Angling, 2019).

In general, the majority of data, available for the reconstruction of the ionosphere and plasmasphere, are Slant Total Electron Content (STEC) measurements, i.e. the integral of the electron density along the line of sight between the GNSS satellite and receiver. Often, STEC measurements provide limited vertical information and hence the modelling of the vertical the electron density distribution is hampered (Dettmering, 2003).

The estimation of the topside ionosphere and plasmasphere poses a particular difficulty since direct electron density measurements are rare and since low plasma densities at these high altitudes contribute only marginally to the STEC measurements. Especially, ground-based STEC measurements are dominated by electron densities within and below the characteristic F2 layer peak. Consequently, information about the plasmasphere can be hardly extracted from ground-based STEC measurements, cf. e.g. Spencer and Mitchell, 2011. Thus, in the presented work, we concentrate on the modeling of the topside part of the ionosphere and plasmasphere and utilize only the space-based STEC measurements.

In this paper, we introduce an Ensemble Kalman Filter to estimate the topside ionosphere and plasmasphere based on space-based STEC measurements. The propagation of the analyzed state vector to the next time step within a Kalman Filter is a tricky point. The majority of the approaches, working with EnKF variants, uses physic-based models for the propagation step (cf. e.g. Elvidge and Angling 2019; Codrescu et al., 2018; Lee et al., 2012). In our work, we investigate the question how the propagation step can be realized, if a physical model is not available or if the usage of a physical model is rejected as computational time consuming. We discretize the ionosphere and the plasmasphere below the GNSS orbit height by 3D voxels, initialize them with electron densities calculated by the NeQuick model and update them with respect to the data. We present different methods how to perform the

https://doi.org/10.5194/angeo-2020-39
Preprint. Discussion started: 23 June 2020

Annales Geophysicae Discussions Open Access EGU

propagation step and assess their suitability for the estimation of electron density. For this purpose, a case study over quiet and perturbed ionospheric conditions in 2015 is conducted, investigating the capability of the estimations to reproduce assimilated STEC as well as to reconstruct independent STEC and electron density measurements.

We organize the paper as follows: Section 2 describes the EnKF with the different propagation methods and the generation of the initial ensembles by the NeQuick model. Section 3 outlines the validation scenario with the applied data sets and section 4 presents the obtained results. Finally, we conclude our work in section 5 and provide an outlook on the next steps.

2 Estimation of the topside ionosphere and plasmasphere by EnKF

2.1 Formulation of the underlying inverse problem

The information about the slant total electron content (STEC), along the satellite-to-receiver ray path s can be obtained from multi-frequency GNSS measurements. In detail, STEC is a function of the electron density Ne along the ray path s, given by

$$STEC_s = \int Ne(h, \lambda, \varphi) ds, \tag{1}$$

where $Ne(h, \lambda, \varphi)$ is the unknown function describing the electron density values depending on altitude h, geographic longitude λ and latitude φ.

The discretization of the ionosphere by a 3D grid and the assumption of a constant electron density function within a fixed voxel allow us the transformation of Eq. (1) into a linear system of equations

$$STEC_s \approx \sum_{i=1}^{K} Ne_i \cdot h_{si} \;\Rightarrow y = Hx + r, \tag{2}$$

where y is the a $m \times 1$ vector of the STEC measurements, x is the vector of unknown electron densities with $x_i = Ne_i$ equals the electron density in the voxel i, h_{si} is the length of the ray path s in the voxel i and r is the vector of measurement errors assumed to be Gaussian distributed with $r \sim N(0, R)$ with expectation 0 and covariance matrix R.

2.2 Background model

As regularisation of the inverse problem in Eq. (2), a background model often provides the initial guess of the state vector x. In this study, we apply the NeQuick model version 2.0.2. The NeQuick model was developed at the International Centre for Theoretical Physics (ICTP) in Trieste/Italy and at the University of Graz/Austria (cf. Hochegger et al. (2000); Radicella and Leitinger (2001); Nava et al. (2008)). We use the daily solar flux index F10.7, to drive the NeQuick model.

2.3 Analysis step

We apply an EnKF to solve the inverse problem defined in Section 2.1. Evensen (1994) introduces the EnKF as an alternative to the standard Kalman Filter (KF) in order to cope with the non-linear propagation dynamics and the large dimension of the state vector and its covariance matrix. In an EnKF, a collection of realisations, called ensembles, represent the state vector x and its distribution.

https://doi.org/10.5194/angeo-2020-39
Preprint. Discussion started: 23 June 2020

Annales Geophysicae Discussions Open Access EGU

Let $X^f = [x_1^f, \dots, x_K^f]$ be a $K \times N$ matrix whose columns are the ensemble members, ideally following the a priori distribution of the state vector x. Further, the observations collected in y are treated as random variables. Therefore, we define a $m \times N$ ensemble of observations $Y = [y_1, y_2, \dots, y_N] \in$ with $y_i = y + \epsilon_i$ and a random vector ϵ_i from the normal distribution $N(0, R)$.

We define the ensemble covariance matrix around the ensemble mean $E(X^f) = \frac{1}{N}\sum_{j=1}^{N} x_j^f$ as follows:

$$P^f = \frac{1}{N-1}\sum_{j=1}^{N}\left\{\left(x_j^f - E(X^f)\right)\cdot\left(x_j^f - E(X^f)\right)^T\right\}. \tag{3}$$

In the analysis step of the EnKF, the a priori knowledge on the state vector x and its covariance matrix is updated by

$$X^a = X^f + P^f H^T (R + H P^f H^T)^{-1} \cdot (Y - H X^f), \tag{4}$$

where the matrix X^a represents the a posteriori ensembles and hence the a posteriori state vector.

For the propagation of the analysed solution to the next time step, we test different propagation models described in Section 2.4. In order to generate the initial ensembles $X^f(t_0)$ we use the NeQuick model and describe the procedure in section 2.5. Keeping in mind that we have to deal with a huge state vector (details are presented in Section 3.1), the big advantage of the EnKF, for the present study, is that there is no need for explicitly calculation of the ensemble covariance matrix (cf. Eq. (3)). Instead, to perform the analysis step in Eq. (4) we follow the implementation suggested by Evensen (2003).

2.4 Considered models for the propagation step

In this section, we introduce the different models investigated to propagate the analysed solution to the next time step. With all of them, we propagate the ensembles 20 minutes in time. These propagation models can be generally described as $X^f(t_{n+1}) = F\left(X^a(t_n)\right) + W_F(t_{n+1}) + \Omega_F(t_{n+1})$.

We applied different approaches to model F, the systematic error W_F and the process noise Ω_F and present in this paper a selection of the most promising variants of them.

2.4.1 Method 1: Rotation

The method Rotation assumes that in magnetic coordinates, the ionosphere remains invariant in space while Earth rotates below it (cf. Angling and Cannon, 2004). Thus, we propagate the analysed ensemble $X^a(t_n)$ from time t_n to the next time step t_{n+1} by:

$$X^f(t_{n+1}) = Rot\left(X^a(t_n)\right) + W_{rot}(t_{n+1}). \tag{5}$$

In detail, to calculate $Rot\left(X^a(t_n)\right)$ the magnetic longitude is changed corresponding to the evolution time $\Delta t = t_{n+1} - t_n$, i.e. 5 degree of longitude per 20 minutes. W_{rot} denotes the systematic error introduced by approximation of the true propagation of X^f by a simple rotation. We tested here the following estimation of W_{rot}:

$$W_{rot}(t_{n+1}) = ratio_{rot}(t_{n+1}) \cdot E\left(Rot\left(X^a(t_n)\right)\right) \cdot \epsilon_{1\times N} \text{ and } ratio_{rot}(t_{n+1}) = \frac{\left(x^b(t_{n+1}) - Rot\left(x^b(t_n)\right)\right)}{3 \cdot Rot\left(x^b(t_n)\right)}, \tag{6}$$

where x^b is the electron density vector calculated by the NeQuick model and $\epsilon_{1\times N}$ is an 1-by-N matrix of ones. The division in the second equation is an element-wise one.

https://doi.org/10.5194/angeo-2020-39
Preprint. Discussion started: 23 June 2020

2.4.2 Method 2: Exponential decay

Here we assume the electron density differences between the voxels of the analysis and the background model to be a first order Gauss-Markov sequence. These differences are propagated in time by an exponential decay function (cf. Nikoukar et al. 2015, Bust and Mitchell, 2008; Gerzen et al., 2015)

$$X^f(t_{n+1}) = X^b(t_{n+1})\cdot \epsilon_{1\times N} + f(t_{n+1})\cdot [X^a(t_n) - X^b(t_n)], \tag{7}$$

where $X^b(t)$ is the ensemble of electron density vectors calculated by the NeQuick model for the time t as described in section 2.5; $f(t_{n+1}) = \exp\left(-\frac{\Delta t}{\tau}\right)$; $\Delta t = t_{n+1} - t_n$; τ denotes the temporal correlation parameter chosen here as 3 hours.

Note: Similar to the method described here, we tested also the application of $Rot([X^a(t_n) - X^b(t_n)])$ instead of $[X^a(t_n) - X^b(t_n)]$ in Eq. (7). The results were similar and are therefore not presented here.

2.4.3 Method 3: Rotation with exponential decay

As third method, we define the propagation model as a combination of the propagation models described in the previous subsections, in particular

$$X^f(t_{n+1}) = x^b(t_{n+1})\cdot \epsilon_{1\times N} + f(t_{n+1})\cdot Rot([X^a(t_n) - x^b(t_n)\cdot \epsilon_{1\times N}]) + W(t_{n+1}) + \sqrt{\frac{\Delta t}{20}}\cdot \Omega_{exp}(t_{n+1}). \tag{8}$$

The systematic error W is estimated as

$$W(t_{n+1}) = f(t_{n+1})\cdot \frac{8}{10}\cdot W_{rot}(t_{n+1}). \tag{9}$$

Thereby f and W_{rot} are defined as in the two sections bevor. The process noise Ω_{exp} is assumed to be white with $\Omega_{exp}(t_{n+1}) = f(t_{n+1})\cdot \Omega_{rot}(t_{n+1}) + \left(1 - f(t_{n+1})\right)\cdot Q_{exp}(t_{n+1})$. Here the matrix Ω_{rot} consists of random realizations of the distribution $N(0, \Sigma^{rot})$ with

$$\Sigma_{ii}^{rot}(t_{n+1}) = \left(ratio_i \cdot \left\{E\left(Rot\left(X^a(t_n)\right)\right)\right\}_i\right)^2, \tag{10}$$

where $ratio_i$ increases continuously depending on the altitude of the voxel i from $\frac{0.5}{100}$ for lower altitudes to $\frac{1}{100}$ for the higher altitudes; $E\left(Rot\left(X^a(t_n)\right)\right)$ denotes the ensemble mean vector. The equations (8) and (10) can be interpreted as follows: for the chosen time step of 20 minutes, the standard deviation of the time model error regarding the voxel i is equal to $\sqrt{\Sigma_{ii}^{rot}(t_{n+1})} = ratio_i \cdot \left\{E\left(Rot\left(X^a(t_n)\right)\right)\right\}_i$, varying between 0.5% and 1% of the corresponding analyzed electron density in the voxel i. In details, we generate at each time step a new vector $\rho_i \sim N(0,1)$ with $\dim(\rho_i) = 100 \times 1$ and calculate to calculate the i-th row ω_i^{rot} of Ω_{rot} by

$$\omega_i^{rot}(t_{n+1}) = \sqrt{\Sigma_{ii}(\Omega_{rot}(t_{n+1}))}\cdot \rho_i(t_{n+1})^T. \tag{11}$$

The matrix $Q_{exp}(t_{n+1})$ consists of random realizations (different for each time step) consistent with the a priori covariance matrix L of the errors of the background $x^b(t_{n+1})$ (cf. Howe and Runciman, 1998). In details: The a priori covariance is assumed to be diagonal and L_{ii} equals the square of 1% of the corresponding background model value. Then the i-th row of Q_{exp} is calculated by Eq. (12):

$$q_i(t_{n+1}) = \sqrt{L_{ii}(t_{n+1})}\cdot \rho_i(t_{n+1})^T. \tag{12}$$

https://doi.org/10.5194/angeo-2020-39
Preprint. Discussion started: 23 June 2020

2.5 Generation of the ensembles

In order to generate the ensembles we vary the F10.7 input parameter of the NeQuick model (cf. Section 2.2). First, we analysed the sensitivity of the NeQuick model on F10.7. Based on the results, we calculate a vector $\boldsymbol{F10.7}(t)$ of the solar radio flux index with $\dim(\boldsymbol{F10.7}(t)\ ) = 100 \times 1$ and $\boldsymbol{F10.7}(t) \sim N\left(\mathrm{F10.7}(t), \frac{3}{100} \cdot \mathrm{F10.7}(t)\right)$ at time t. The vector $\boldsymbol{F10.7}$ serves as input for the NeQuick model to calculate the 100 ensembles of X^b during the considered period and the initial guess of the electron densities $X^f(t_0)$.

An example on the variation of the generated ensembles is provided by **Figure 1**. Particularly, we show in this figure the distribution of the differences between the ensemble of electron densities $X^b(t)$ and the NeQuick model values for DOYs 041 and 076. The residuals are depicted for a selected altitude and chosen UT times, presented through different colors (cf. subfigure history). In addition, the mean, the standard deviation (STD) and the root mean square (RMS) of the residuals are presented in the subplots.

3 Validation scenario

Within this study, the EnKF with the different propagation methods is applied and validated for the tomography of the topside ionosphere and plasmasphere. Particularly, two periods with quiet (DOY 041-059, 2015) and perturbed (DOY 074-079, 2015) ionospheric conditions are analysed. In this scope, we investigate the ability to reproduce assimilated STEC as well as to estimate independent STEC measurements and in-situ electron density measurements of the Swarm Langmuir Probes (LP).

In addition, we apply the tomography approach SMART+ (Gerzen and Minkwitz, 2016 and Gerzen et al., 2017) to provide a benchmark. For SMART+ the number of iterations at each time step is set to 25 and the correlation coefficients are chosen as described in Gerzen and Minkwitz (2016).

3.1 Reconstruction area

We estimate the electron density over the entire globe with a spatial resolution of 2.5 degrees in latitude and longitude. Altitudes between 430 km and 20 200 km are reconstructed where the resolution equals 30 km for altitudes from 430 km to 1000 km and decreases exponentially with increasing altitude for altitudes above 1000 km, i.e. in total 42 altitudes. Consequently, the number of unknowns is $K = 217728$. The temporal resolution is set to 20 minutes.

3.2 Ionospheric conditions in the considered periods

We use the solar radio flux F10.7, the global planetary 3h index Kp and the geomagnetic disturbance storm time (DST) index to characterize the ionospheric conditions during the periods of DOY 041-059 and DOY 074-079 2015. In the February period (DOY 041-059, 2015) the ionosphere is evaluated as quiet with F10.7 between 108 and 137 sfu, a Kp index below 6 and DST values between 20 and -60 nT. The 17-th of March (DOY 076) 2015 is known as the St. Patrick's Day storm. The F10.7 value equals ~116 sfu on DOY 075 and ~113 sfu on DOY076, the Kp index is below 5 on DOY 075 and increases to 8 on DOY 076; DST drops down to -200nT on DOY 076.

https://doi.org/10.5194/angeo-2020-39
Preprint. Discussion started: 23 June 2020

Annales Geophysicae Discussions

3.3 Data

3.3.1 STEC measurements

As input for the tomography approaches and for the validation, we use space-based calibrated STEC measurements of the following satellite missions: COSMIC satellites, Swarm satellites, TerraSAR-X, MetOpA and MetOpB, GRACE LEO satellites. Please note that in 2015, the orbit height of the COSMIC and MetOp satellites is ~800 km, the orbit height of the Swarm B and TerraSAR-X satellites is ~500 km and the one of the Swarm C satellite ~460 km. The STEC measurements of Swarm A and GRACE are used only for the validation.

The STEC measurements of the Swarm satellites are acquired from https://swarm-diss.eo.esa.int/ and the STEC measurements of the other satellite missions are downloaded from http://cdaac-www.cosmic.ucar.edu/cdaac/tar/rest.html. Both data provider supply also information on the accuracy of the STEC data. We utilize this information to fill the covariance matrix R of the measurement errors.

3.3.2 In-situ electron density measurements from the Swarm Langmuir Probes

The LPs on board the Swarm satellites provide in-situ electron density measurements with a time resolution of 2 Hz. For the present study, the LP in-situ data are acquired from https://swarm-diss.eo.esa.int/. Further, information on the pre-processing of the LP data is made available.

Lomidze et. al (2018) assess the accuracy and reliability of the LP data (December 2013 to June 2016) by nearly coincident measurements from low- and middle-latitude incoherent scatter radars, low-latitude ionosondes, and COSMIC satellites, which cover all latitudes. The comparison results for each Swarm satellite are consistent across these different measurement techniques. The results show that the Swarm LPs underestimate the electron density systematically by about 10%.

4 Results

In this section, the different methods are presented with the following color code: blue for the method Rotation, green for the method Exponential decay, light blue for the method Rotation with exponential decay, magenta for NeQuick and red for SMART+. The legends in the figures are the following: “Rot” for the method Rotation, “Exp” for the method Exponential decay, “Rot and Exp” for the method Rotation with exponential decay.

4.1 Reconstructed electron densities

At the end of each EnKF analysis step, we have, for each of the considered methods, 100 ensembles representing the electron density values within the voxels. The EnKF reconstructed electron densities are then calculated as the ensemble mean. The top subplots of **Figure 2** present the electron densities at DOY 076, 19:00 UT, reconstructed by the method Rotation with exponential decay. The left hand side subplot shows horizontal layers of the topside ionosphere at different heights between 490 and 827 km. The right hand side subplot shows the plasmasphere for altitudes between 827 and 2400 km at chosen longitudes. The bottom line subplots show the vertical TEC maps deduced from the 3D electron density in the considered altitude range between 430 and 20200 km for the same time stamp. The left hand side subplot show the reconstructed values and the right hand side VTEC is deduced from the NeQuick model calculated electron density. The reconstructed results are a bit higher than NeQuick ones.

Figure 3 displays method Rotation reconstructed electron density layers at different heights between 490 and 827 km (left) and vertical TEC map deduced from the reconstructed 3D electron density in the altitude range between 430 and 20200 km (right) for the same DOY 076, at 19:00 UT. The method Rotation delivers much higher values than NeQuick. All reconstructed values seems to be plausible, showing as expected the crest region, low electron densities in the Polar regions, etc.

4.2 Plausibility check by comparison with assimilated STEC

In this chapter, we check the ability of the methods to reproduce the assimilated STEC measurements. For that purpose, we calculate STEC along a ray path j, for all ray path geometries, using the estimated 3D electron densities, denoted as $STEC_j^{est}$, and compare them with the measured STEC, $STEC_j^{meas}$, used for the reconstruction. Then the mean deviation $\Delta\boldsymbol{STEC}$ between the measurements $STEC_j^{meas}$ and the estimate $STEC_j^{est}$ is calculated for each of the considered methods according to

$$\Delta\boldsymbol{STEC}(t_n) = \frac{1}{m}\sum_{j=1}^{m}\left(\left|STEC_j^{meas}(t_n) - STEC_j^{est}(t_n)\right|\right), \tag{13}$$

where m = number of assimilated measurements. $\Delta\boldsymbol{STEC}$ is calculated at each epoch t_n. In terms of the notation used for the Eqs. (1) - (4), we can reformulate the above formula for the mean deviation as

$$\Delta\boldsymbol{STEC}(t_n) = \frac{1}{m}\sum_{j=1}^{m}\left(\left|y_j(t_n) - E\left(X_a(t_n)\right)^T \cdot H_j\right|\right), \text{ with } H_j = j\text{-th row of } H. \tag{14}$$

Further, we consider the **RMS** of the deviations, in detail

$$\boldsymbol{RMS}(t_n) = \sqrt{\frac{1}{m}\sum_{j=1}^{m}\left(\left|STEC_j^{meas}(t_n) - STEC_j^{est}(t_n)\right|\right)^2}. \tag{15}$$

To calculate $\Delta\boldsymbol{STEC}$ and $\boldsymbol{RMS}$, the same measurements are used as for the reconstruction. In this sense, the results presented in **Figure 4** - **Figure 8** can serve as a plausibility check, testing the ability of the methods to reproduce the assimilated TEC.

Figure 4 depicts the distribution of the residuals, left subfigure for the quiet period, right subfigure for the perturbed period. The corresponding residual median, standard deviation (STD) and root mean square (RMS) values are also presented in the figure. It is worth to mention here that during the quiet period, the measured STEC is below 150 TECU. For all DOYs of the perturbed period, except DOY 076, the measured STEC is below ~130 TECU. On DOY 076, the STEC values rise up to 370 TECU.

The NeQuick model seems to underestimate the measured topside ionosphere and plasmasphere STEC during both periods. During both periods, SMART+ seems to perform best, followed by the method Rotation. However, the last one produces higher STD and RMS values. Compared to the NeQuick residuals, SMART+ is able to reduce the median of the residuals by up to 86% during the perturbed and up to 79% during the quiet period. The RMS is reduced by up to 48% and the STD by up to 41%. Rotation reduces the NeQuick median by up to 83%, the RMS by up to 27%, the STD value is almost on the same level as for NeQuick. The method Exponential decay is able to decrease the median of the NeQuick residuals by up to 54%, the RMS by up to 25%, and the STD values by up to 13%. The method Rotation with exponential decay performs similar to the NeQuick model.

Interestingly, the median values are higher during the quiet period, while during the perturbed period the RMS and STD values are significantly higher. The reason therefore is probably that the assimilated STEC values have in

https://doi.org/10.5194/angeo-2020-39
Preprint. Discussion started: 23 June 2020

average lower magnitude during the days in the perturbed period, compared to those during the quiet period (which explains the lower median), except the storm DOY 076, while on DOY 076 they are significantly higher (which explains the higher STD and RMS).

Figure 5 and **Figure 6** plot $\Delta\boldsymbol{STEC}$ values versus time for the selected periods. Noticeable is the increase of $\Delta\boldsymbol{STEC}$ during the storm on DOY 76. On the rest of the period, $\Delta\boldsymbol{STEC}$ is below eight TECU. During both periods, SMART+ generates the lowest $\Delta\boldsymbol{STEC}$ values. $\Delta\boldsymbol{STEC}$ of the methods Rotation and Exponential decay are in most of the cases higher than SMART+ delta STEC values and lower than the NeQuick model. $\Delta\boldsymbol{STEC}$ of the method Rotation with exponential decay is similar to the NeQuick model.

Figure 7 and **Figure 8** present the distribution of $\Delta\boldsymbol{STEC}$ and the $\boldsymbol{RMS}$ error (cf. Eq. (14)) for the quiet and perturbed periods respectively. **Figure 7** confirms the conclusions we draw so far from **Figure 4** and **Figure 5** . SMART+ delivers the lowest $\Delta\boldsymbol{STEC}$ and $\boldsymbol{RMS}$ values, followed by the method Rotation and then by the method Exponential decay. Rotation with exponential decay performs similar to the NeQuick model. For the perturbed period, again SMART+ delivers the lowest $\Delta\boldsymbol{STEC}$ and $\boldsymbol{RMS}$ statistics, followed by the Exponential decay and the Rotation with similar results.

4.3 Validation with independent space-based sTEC data

In order to validate the methods with respect to their capability to estimate independent STEC, the LEO satellites Swarm A and GRACE are chosen. The STEC measurements of these satellites are not assimilated by the tested methods. It is to mention here that 2015 the Swarm A satellite was flying site on site with the Swarm C satellite at around 460 km height. The height of the GRACE orbit was around 450 km. All satellites were flying on almost polar orbits.

For each of the tree LEOs, the residuals between $STEC^{meas}$ and $STEC^{est}$ are calculated and denoted as $dTEC = STEC^{meas} - STEC^{est}$. Further, the absolute values of the residuals $|dTEC|$ are considered.

In general, for the quiet period, the STEC measurements of Swarm A vary below 105 TECU and for the second period below 170 TECU. For the GRACE satellite, the STEC measurements are below 282 TECU for the quiet period and below 264 TECU for the second period.

Figure 9 and **Figure 10** display the histograms of the STEC residuals during the quiet period for Swarm A and GRACE respectively. Presented are the distributions of the residuals $dTEC$ and the absolute residuals $|dTEC|$. Also plotted are the median, STD and RMS of the corresponding residuals. **Figure 11** and **Figure 12** depict the histograms of the STEC residuals during the perturbed period.

Again, the NeQuick model seems to underestimate the measured STEC during both periods for GRACE and Swarm A satellites. Compared to the NeQuick model, during both periods, the methods SMART+ and Exponential decay decrease the residuals and the absolute residuals between measured and estimated STEC for both GRACE and Swarm A satellites. The method Rotation with exponential decay performs for both periods very similar to the NeQuick model. The performance of the method Rotation is partly even worse than the one of the background model. Our impression is that the number and the distribution of the assimilated measurements is too small and angle limited to be sufficient to dispense with a background model, as is the case with the Rotation method, which uses the model only for the estimation of the systematic error.

https://doi.org/10.5194/angeo-2020-39
Preprint. Discussion started: 23 June 2020

Regarding the STEC of Swarm A, the lowest residuals and the most reduction in comparison to the NeQuick model, are achieved by SMART+. The median and the STD of the SMART+ residuals are ~0.3 TECU and ~3.4 TECU resp. for quiet and ~ 0.7 TECU and ~7 TECU for the perturbed period. Compared to the NeQuick model, the absolute median value is reduced up to 64% by SMART+ during the quiet and by up to 61% during the perturbed period. The STD value is decreased by up to 47% during the quiet and up to 29% during the storm period. The second lowest residuals are achieved by the Exponential decay - here the median of the residuals is around 0.2 TECU for quiet and around 0.8 TECU for the perturbed period.

Regarding the STEC of GRACE during the quiet period, the lowest residuals and the most reduction in comparison to background, are achieved by the Exponential decay, followed by SMART+. Exponential decay reduces the background absolute median value by up to 26% and the STD value by up to 28%. The median of the residuals is around 0.2 TECU. For SMART+, the median of the residuals is around 2.9 TECU. During the perturbed period, SMART+ reduces the absolute median at most by 17% and the STD by 9%, the Exponential decay does not reduce the absolute median, compared to NeQuick, but it reduces the absolute STD value by 23%. The median of the residuals are around -0.5 TECU for Exponential decay and around 0.8 TECU for SMART+.

Comparing between quiet and storm conditions, in general an increase of RMS and STD of the residuals is observable for the NeQuick model and all tomography methods regarding both satellites.

4.4 Validation with independent LP in-situ electron densities

In this section, we further extend our analyses to the validation of the methods with independent LP in-situ electron densities of the three Swarm satellites. According to the locations of the LP measurements, the estimated electron density values are interpolated from the 3D electron density reconstructions. For each satellite, the measured electron density Ne^{meas} is compared to the estimated one Ne^{est}. In particular we calculate the residuals $dNe = Ne^{meas} - Ne^{est}$, the absolute residuals $|dNe|$, the relative residuals $dNe_{rel} = \frac{dNe}{Ne^{meas}} \cdot 100\%$ and the absolute relative residuals $|dNe_{rel}|$.

Figure 13 depicts the distribution of the residuals dNe for the quiet period along with the median, STD and RMS values. Each of the three subplots presents one of the Swarm satellites. In **Figure 14** the histograms of $|dNe|$ and $|dNe_{rel}|$ are given for the same period. In **Figure 14** we do not separate the values for the different satellites, because these are similar. **Figure 15** and **Figure 16** show the corresponding histograms for the perturbed period.

The electron densities of the NeQuick model are in median slightly higher than the LP in-situ measurements for all three satellites during both periods. The median and STD values for the $|dNe_{rel}|$ residuals produced by NeQuick are ~33% and ~38% resp. during the quiet period. For the perturbed period, we observe higher median and STD values of ~45% and ~56%, resp. The increase of the RMS and STD values of the absolute residuals is also visible for all the considered reconstruction methods.

The methods SMART+ and Rotation with exponential decay follow the trend of the model and show similar distributions in **Figure 13** and **Figure 15**. Comparing these two methods with the NeQuick model, the performance of SMART+ is slightly better reducing the median of the absolute and absolute relative residuals by up to 8%. Further, during both periods, SMART+ reduces the STD values of the $|dNe|$ values by up to 23%. However, the STD and RMS values of the $|dNe_{rel}|$ residuals for SMART+ during the quiet period are higher than those of the NeQuick model. The median and STD values of the $|dNe_{rel}|$ residuals for SMART+ are ~30% and ~43% resp.

https://doi.org/10.5194/angeo-2020-39
Preprint. Discussion started: 23 June 2020

Annales Geophysicae Discussions

during quiet and higher during perturbed period, namely ~43% and ~53% resp. The statistics of the methods Exponential decay and Rotation are worse than those of NeQuick.

5 Summary and conclusions

In this paper, we focus on the assessment of three different propagation methods for an Ensemble Kalman Filter approach in the case that a physical propagation model is not available or discarded due to computational burden. We validate these methods with independent STEC observations of the satellites GRACE and Swarm A and with independent Langmuir probes data of the three Swarm satellites. The methods are compared to the algebraic reconstruction method SMART+, serving as a benchmark and to the NeQuick model for periods of the year 2015 covering quiet to perturbed ionospheric conditions. This work is carrying out our first case study in this regard.

Overlooking all the validation results, the methods SMART+ and Exponential decay reveal the best performance with the lowest residuals. In general, the method Rotation with exponential decay follows the trends of the NeQuick model. One significant difference between the investigated reconstruction approaches is that Rotation, as the only one of considered methods, uses the background information only for the estimation of the systematic error. The number of the assimilated measurements is small compared to the number of unknowns, additionally the distribution of measurements is uneven and angle limited. We assume these are the main reasons, why the method Rotation reproduces the assimilated STEC data well, but exhibits degraded results in comparisons with independent data.

In summary, the comparison with the assimilated STEC show that during both periods all methods reduce successfully the median, RMS and STD values of the STEC residuals in comparison to the background model. SMART+ performs at best improving the statistics of the NeQuick model by up to 86%, followed by the method Rotation, decreasing the median of the residuals by up to 83%. The method Exponential decay lowers the median by up to 55%, but the STD values stay almost on the same level as for the NeQuick model.

Regarding the ability to estimate independent STEC measurements, the methods SMART+ and Exponential decay reduce the independent STEC residuals by up to 64% for Swarm A and 28% for GRACE, compared to the NeQuick model. SMART+ generates the smallest residuals for the STEC measurements of Swarm A and Exponential decay performs at best for STEC measurements of GRACE.

Concerning the estimation of independent electron density data, SMART+ shows the best results, reducing the background statistics of the absolute residuals by up to 23%. The median and STD values of the absolute residuals $|dNe_{rel}|$ for SMART+ are ~30% and ~43% resp. during quiet and higher, namely ~43% and ~53% resp. during perturbed period. The distributions of the residuals produced by Rotation with exponential decay are similar to the ones of the NeQuick model. In general, all the considered methods generate relatively high residuals. It should be noted here that the independent electron density measurements are located at the lower edge of the reconstructed area and all the assimilated measurements are located above. Additionally, as already mentioned in Section 3.3.2, Swarm LPs was found to underestimate the true electron density systematically. This could be the second reason, why the reconstructions, based on the STEC, do not match the LPs electron densities. To get better results for the lower altitudes, it might be necessary to apply a kind of anchor point from below within the reconstruction procedure. We plan to utilise therefor the Swarm LPs electron denisty measurements themselves.

Further, to get a comprehensive concluding impression of the performance of the investigated methods and to get an insight in the ability of the methods for correct characterization of the electron density profile shapes, we start to work on comparisons with independent electron density data, located in the plasmasphere and with coherent scatter radar data.

Furthermore, a pre-adjustment of the background model, e.g. in terms of F2 layer characteristics or the plasmapause location, may be helpful to improve the reconstruction results (cf. e.g. Bidaine and Warnant, 2010, Gerzen et. al., 2017).

Acknowledgements

We thank the NOAA (ftp://ftp.ngdc.noaa.gov/STP/GEOMAGNETIC_DATA/INDICES/) and WDC Kyoto (http://wdc.kugi.kyoto-u.ac.jp/dstdir/index.html) for making available the geo-related data, F10.7, Kp and DST indices. We are grateful to the European Space Agency for providing the Swarm data (https://swarm-diss.eo.esa.int/) and to the CDAAC: COSMIC Data Analysis and Archive Center for providing the STEC data of several LEO satellites (http://cdaac-www.cosmic.ucar.edu/cdaac/tar/rest.html). Additionally, we express our gratitude to the Aeronomy and Radiopropagation Laboratory of the Abdus Salam International Centre for Theoretical Physics Trieste/Italy for providing the NeQuick version 2.0.2 for scientific purposes. This study was performed as part of the MuSE project (https://gepris.dfg.de/gepris/projekt/273481272?language=en), funded by the DFG as a part of the Priority Programme "DynamicEarth", SPP-1788.

References

Angling, M. J.: First assimilation of COSMIC radio occultation data into the Electron Density Assimilative Model (EDAM), Ann. Geophys., 26, 353-359, 2008.

Angling, M. J. and Cannon, P. S.: Assimilation of radio occultation measurements into background ionospheric models, Radio Sci., 39, RS1S08, doi:10.1029/2002RS002819, 2004.

Banville, S.: Improved convergence for GNSS precise point positioning. Ph.D. dissertation, Department of Geodesy and Geomatics Engineering, Technical Report No. 294, University of New Brunswick, Fredericton, New Brunswick, Canada, 2014.

Bidaine B. and R. Warnant: Assessment of the NeQuick model at mid-latitudes using GNSS TEC and ionosonde data, Adv. Space Res., 45, 1122-1128, 2010.

Bilitza, D., L.-A. McKinnell, B. Reinisch, and T. Fuller-Rowell: The International Reference Ionosphere (IRI) today and in the future, J. Geodesy, 85:909-920, DOI 10.1007/s00190-010-0427-x, 2011.

Bust, G. S., and C. N. Mitchell: History, current state, and future directions of ionospheric imaging, Rev. Geophys., 46, RG1003, doi:10.1029/2006RG000212, 2008.

Codrescu, S. M., M. V. Codrescu, M. Fedrizzi: An Ensemble Kalman Filter for the thermosphere-ionosphere.Space Weather, 16, 57–68, https://doi.org/10.1002/2017SW001752, 2018.

Dettmering D.: Die Nutzung des GPS zur dreidimensionalen Ionosphärenmodellierung. PhD Thesis, University of Stuttgart, http://elib.uni-stuttgart.de/opus/volltexte/2003/1411/, 2003.

Elvidge, S., and M. J. Angling: Using the local ensemble Transform Kalman Filter for upper atmospheric modelling, J. Space Weather Space Clim., 9, A3, https://doi.org/10.1051/swsc/2019018, 2019.

Evensen, G.: Sequential data assimilation with a nonlinear quasi-geostrophic model using Monte Carlo methods to forecast error statistics, J. Geophys. Res., 99 (C5), 10143– 10162, doi:10.1029/94JC00572, 1994.

Evensen, G.: The Ensemble Kalman Filter: theoretical formulationand practical implementation, Ocean Dynamics, 53, 343-367, DOI 10.1007/s10236-003-0036-9, 2003.

Howe, B. M., K Runciman, J. A. Secan, Tomography of the ionosphere: Four-dimensional simulations, Radio Sci., 33, 1, 109-128, 1998.

Gerzen, T., Minkwitz, D., and Schlueter, S.: Comparing different assimilation techniques for the ionospheric F2 layer reconstruction, J. Geophys. Res.-Space, 120, 6901–6913, doi:10.1002/2015JA021067, 2015.

https://doi.org/10.5194/angeo-2020-39
Preprint. Discussion started: 23 June 2020

Annales Geophysicae Discussions

Gerzen, T. and D. Minkwitz, Simultaneous multiplicative column normalized method (SMART) for the 3D ionosphere tomography in comparison with other algebraic methods, Ann. Geophys., 34, 97-115, doi: 10.5194/angeo-34-97-2016, 2016.

Gerzen, T., V. Wilken, D. Minkwitz, M. Hoque, S. Schlüter: Three-dimensional data assimilation for ionospheric reference scenarios, Ann. Geophys., 35, 203-215, doi:10.5194/angeo-35-203-2017, 2017.

Heise, S., N. Jakowski, A. Wehrenpfennig, Ch. Reigber, H. Lühr: Sounding of the topside ionosphere/plasmasphere based on GPS measurements from CHAMP: Initial results, Geophys. Res. Letters, 29(14), doi: 10.1029/2002GL014738, 2002.

Hernandez-Pajares, M., J.M. Juan, J. Sanz: New approaches in global ionospheric determination using ground GPS data. J Atmos Solar Terr Phys, 61: 1237-1247, 1999.

Hochegger G., Nava B., Radicella S.M., and R. Leitinger: A Family of Ionospheric Models for Different Uses, Phys. Chem. Earth Part C Solar Terres Planet Sci, 25, 307-310, doi:10.1016/S1464-1917(00)00022-2, 2000.

Howe B., K. Runciman: Tomography of the ionosphere: Four-dimensional simulations, Radio Sci., 33, 1, 09-128, 1998.

Lee, I. T., T. Matsuo, A. D. Richmond, J. Y. Liu, W. Wang, C. H. Lin, J. L. Anderson, M. Q. Chen: Assimilation of FORMOSAT-3/COSMIC electron density profiles into a coupled thermosphere/ionosphere model using ensemble Kalman filtering, JGR, 117, A10, https://doi.org/10.1029/2012JA017700, 2012.

Liang, W., M. Limberger, M. Schmidt, D. Dettmering, U. Hugentobler, D. Bilitza, N. Jakowski, M.M. Hoque, V. Wilken, T. Gerzen: Regional modeling of ionospheric peak parameters using GNSS data - an update for IRI. Adv. Space Res., 55(8), 1981-1993, 10.1016/j.asr.2014.12.006, 2015.

Liang, W., M. Limberger, M. Schmidt, D. Dettmering, U. Hugentobler: Combination of ground- and space-based GPS data for the determination of a multi-scale regional 4-D ionosphere model. In: Rizos C., Willis P. (Eds.) IAG 150 Years, IAG Symposia, 143, 751-758, 10.1007/1345_2015_25, 2016.

Lomidze, L., L. Scherliess, R. W. Schunk: Magnetic meridional winds in the thermosphere obtained from Global Assimilation of Ionospheric Measurements (GAIM) model, JGR: Space Physics, 120, 9, 8025-8044, https://doi.org/10.1002/2015JA021098, 2015.

Lomidze, L., D. J. Knudsen, J. Burchill, A. Kouznetsov, S. C. Buchert: Calibration and validation of Swarm plasma densities and electron temperatures using ground-based radars and satellite radio occultation measurements, Radio Sci., 53, 15– 36, https://doi.org/10.1002/2017RS006415, 2018.

Minkwitz, D., K.G. van den Boogaart, T. Gerzen, M.M. Hoque: Tomography of the ionospheric electron density with geostatistical inversion, Ann. Geophys., 33, 1071–1079, https://doi.org/10.5194/angeo-33-1071-2015, 2015.

Minkwitz, D., K. G. van den Boogaart, T. Gerzen, M. Hoque, M. Hernández-Pajares: Ionospheric tomography by gradient enhanced kriging with STEC measurements and ionosonde characteristics, Ann. Geophys., 34, 999-1010, doi:10.5194/angeo-34-999-2016, 2016.

Nava B., P. Coisson, and S.M. Radicella: A new version of the NeQuick ionosphere electron density model, J. Atmos. Sol-Terr. Phy., 70, 1856-1862, doi:10.1016/j.jastp.2008.01.015, 2008.

Nikoukar, R., G. Bust, D. Murr: Anovel data assimilation technique for the plasmasphere, J. Geophhys. Res., Space Physics, 120, 8470-8485, doi:10.1002/2015JA021455, 2015.

Odijk, D.: Precise GPS positioning in the presence of ionospheric delays. Publications on geodesy, Vol. 52. The Netherlands Geodetic Commission, Delft. ISBN-13: 978 90 6132 278 8, 2002.

Olivares-Pulido G., M. Terkildsen, K. Arsov, P.J.G. Teunissen, A. Khodabandeh, V. Janssen: A 4D tomographic ionospheric model to support PPP-RTK, Journal of Geodesy, 93, 9, 1673-1683, https://doi.org/10.1007/s00190-019-01276-4, 2019.

Radicella S. M., and R. Leitinger: The evolution of the DGR approach to model electron density profiles, Adv. Space. Res., 27, 35-40, doi:10.1016/S0273-1177(00)00138-1, 2001.

Schaer, S.: Mapping and predicting the Earth's ionosphere using the global positioning system. Ph.D. dissertation, Astron Institute, University of Bern, Berne, 1999.

Scherliess, L., D. C. Thompson, R. W. Schunk: Ionospheric dynamics and drivers obtained from a physicsbased data assimilation model, Radio Sci., 44, RS0A32, doi:10.1029/2008RS004068, 2009.

Schmidt, M., D. Bilitza, C. Shum, C. Zeilhofer: Regional 4-D modelling of the ionospheric electron density. Adv Space Res 42: 782790. https://doi.org/10.1016/j.asr.2007.02.050, 2008.

Schmidt, M., D. Dettmering, F. Seitz: Using B-spline expansions for ionosphere modeling. In: Freeden W., Nashed M.Z., Sonar T. (Eds.) Handbook of Geomathematics (Second Edition), 939-983, Springer, 10.1007/978-3-642-54551-1_80, 2015.

Schunk, R. W., et al.: Global Assimilation of Ionospheric Measurements (GAIM), Radio Sci., 39, RS1S02, doi:10.1029/2002RS002794, 2004.

https://doi.org/10.5194/angeo-2020-39
Preprint. Discussion started: 23 June 2020

Annales Geophysicae
Discussions

Schunk, R. W., L. Scherliess, V. Eccles, L. C. Gardner, J. J. Sojka, L. Zhu, X. Pi, A. J. Mannucci, M. Butala, B. D. Wilson, A. Komjathy, C. Wang, G. Rosen: Space weather forecasting with a Multimodel Ensemble Prediction System (MEPS), Radio Sci., 51, 1157–1165, doi:10.1002/2015RS005888, 2016.

Spencer, P. S. J., C. N. Mitchell: Imaging of 3-D plasmaspheric electron density using GPS to LEO satellite differential phase observations, Radio Sci., 46, RS0D04, https://doi.org/10.1029/2010RS004565, 2011.

Wang, C., G. Hajj, X. Pi, I. G. Rosen, B. Wilson: Development of the Global Assimilative Ionospheric Model, Radio Sci., 39, RS1S06, doi:10.1029/2002RS002854, 2004.

Wen, D., Y. Yuan, J. Ou, X. Huo, K. Zhang: Three-dimensional ionospheric tomography by an improved algebraic reconstruction technique, GPS Solut., 11, 251–258, doi:10.1007/s10291-007-0055-y, 2007.

Wen, D., D. Mei, Y. Du: Adaptive Smoothness Constraint Ionospheric Tomography Algorithm, Sensors (Basel), 20, 8, doi: 10.3390/s20082404, 2020.

Zeilhofer, C.: Multi-dimensional B-spline Modeling of Spatio-temporal Ionospheric Signals: DGK. Series A, 123, München, 2008.

Zeilhofer, C., M. Schmidt, D. Bilitza, C. K. Shum: Regional 4-D modeling of the ionospheric electron density from satellite data and IRI, Adv. Space Res., 43, 2009.

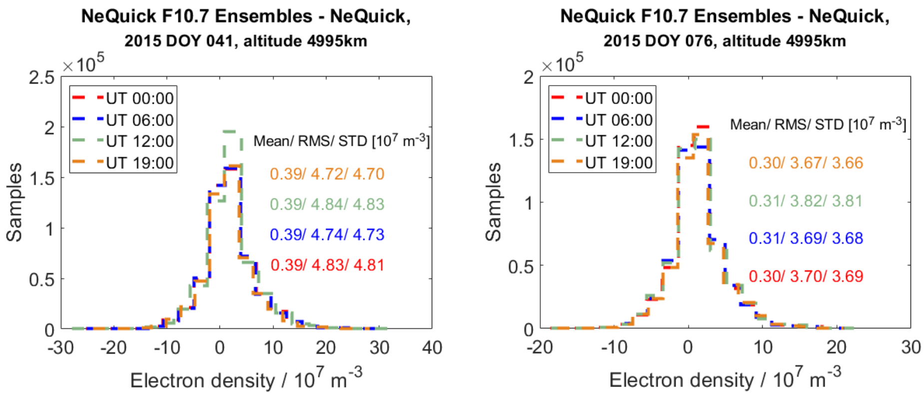

Figure 1: The distribution of the ensemble residuals for a chosen altitude and selected UT times, for all latitudes, longitudes. Left – for DOY 041, right – for DOY 076.

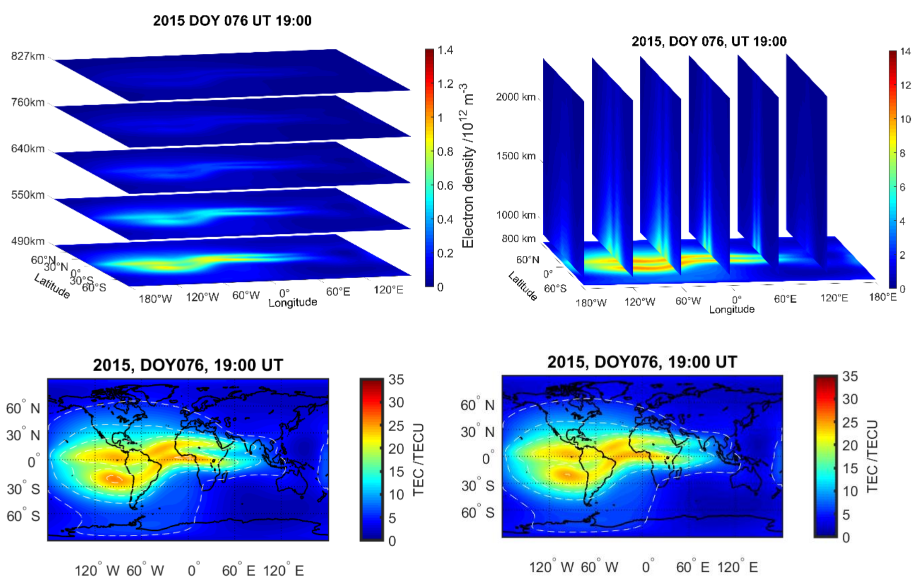

https://doi.org/10.5194/angeo-2020-39
Preprint. Discussion started: 23 June 2020

Annales Geophysicae Discussions

Figure 2: Subfigures top: Rotation with exponential decay reconstructed electron density represented by layers at different heights between 490 and 827 km (left) and at chosen longitudes for altitudes between 827 and 2400 km (right). Subfigures bottom: The vertical TEC map deduced from the reconstructed (left) and NeQuick-modeled (right) 3D electron density in the altitude range between 450 and 20200 km.

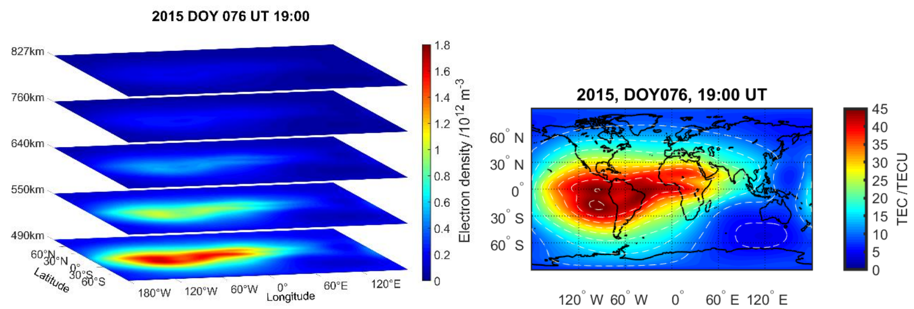

Figure 3: Subfigures top: Method Rotation reconstructed electron density represented by layers at different heights between 490 and 827 km (left) and vertical TEC map deduced from the reconstructed 3D electron density in the altitude range between 450 and 20200 km (right).

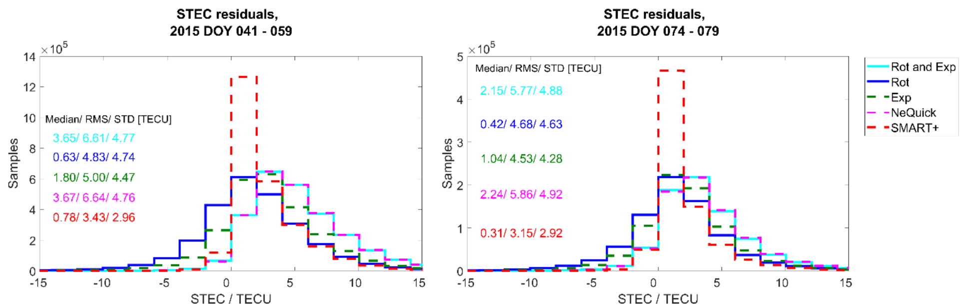

Figure 4: Plausibility check – distributions of the STEC measured – STEC estimated residuals. Left subfigure depicts residuals of the quiet period, right subfigure for the perturbed period.

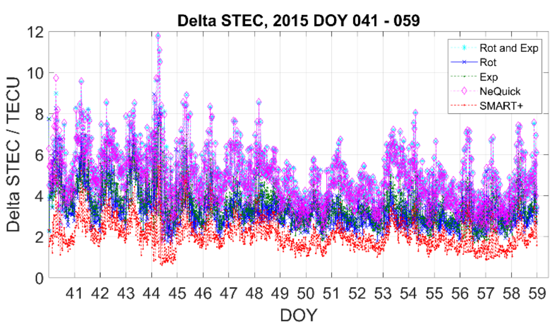

Figure 5: Plausibility check for the quiet period – $\Delta STEC$ values versus time.

https://doi.org/10.5194/angeo-2020-39
Preprint. Discussion started: 23 June 2020

Annales Geophysicae Discussions
Open Access
EGU

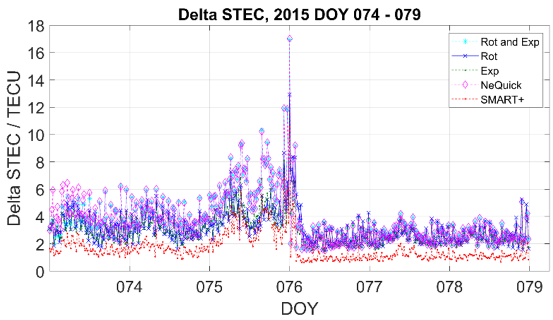

Figure 6: Plausibility check for the perturbed period – $\Delta STEC$ values versus time.

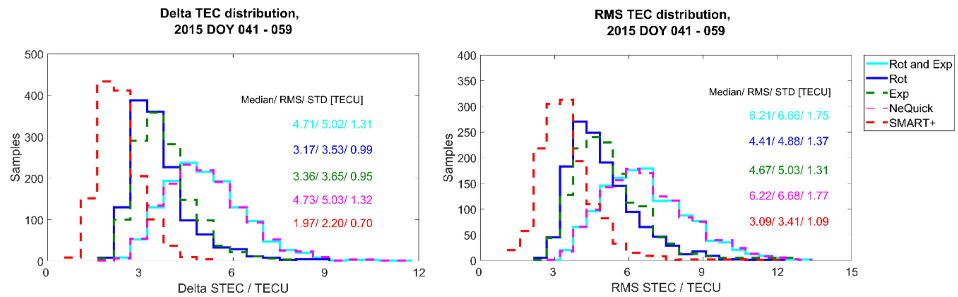

Figure 7: Plausibility check for the quiet period – distributions of the delta TEC (left) and RMS (right) values.

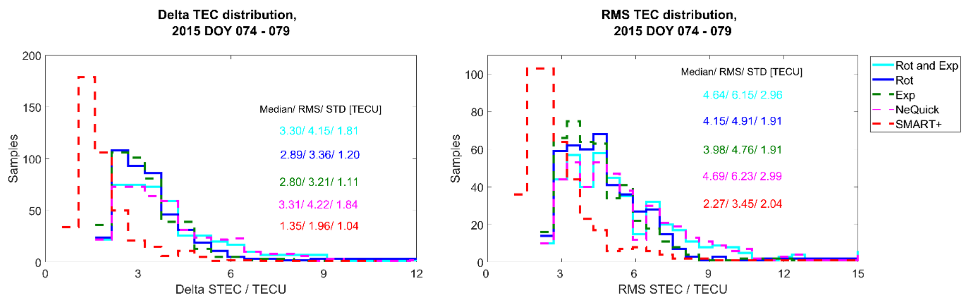

Figure 8: Plausibility check for the perturbed period – distributions of the delta TEC (left) and RMS (right) values.

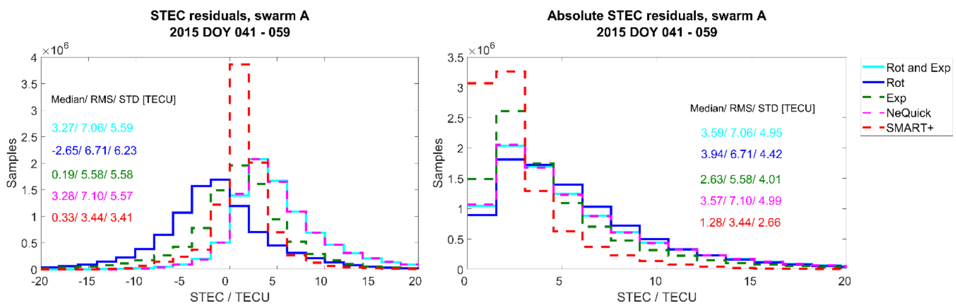

https://doi.org/10.5194/angeo-2020-39
Preprint. Discussion started: 23 June 2020

Annales Geophysicae Discussions

Figure 9: Histograms of the STEC residuals (left) and absolute residuals (right) during the quiet period, for Swarm A.

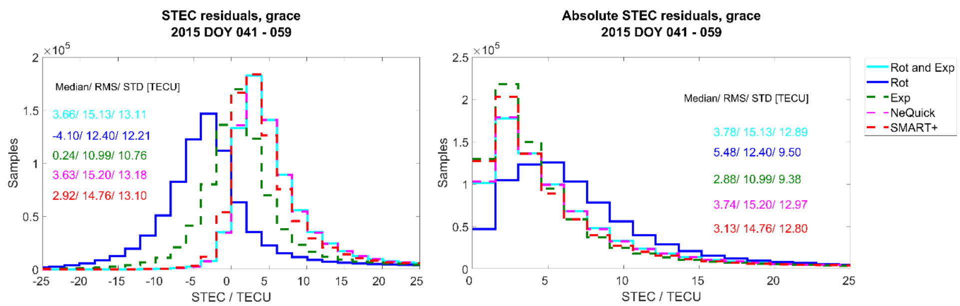

Figure 10: Histograms of the STEC residuals (left) and absolute residuals (right) during the quiet period, for GRACE.

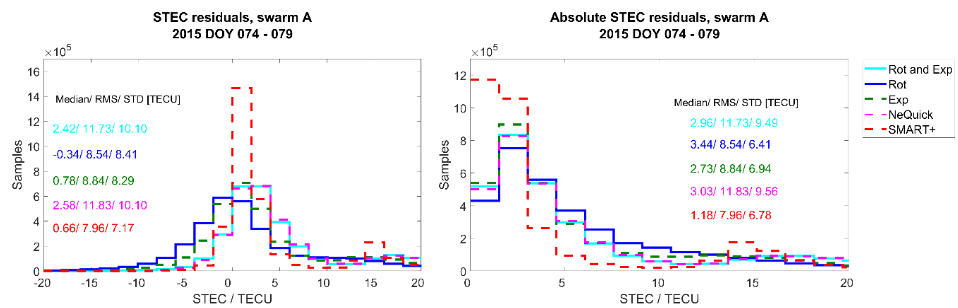

Figure 11: Histograms of the STEC residuals (left) and absolute residuals (right) during the perturbed period, for Swarm A.

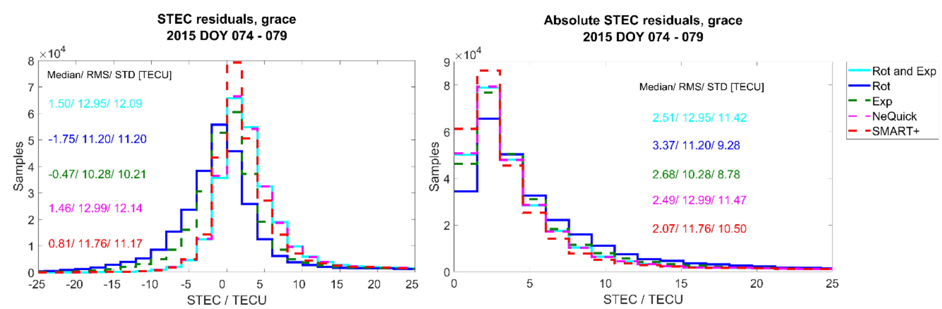

Figure 12: Histograms of the STEC residuals (left) and absolute residuals (right) during the perturbed period, for GRACE.

https://doi.org/10.5194/angeo-2020-39
Preprint. Discussion started: 23 June 2020

Annales Geophysicae Discussions

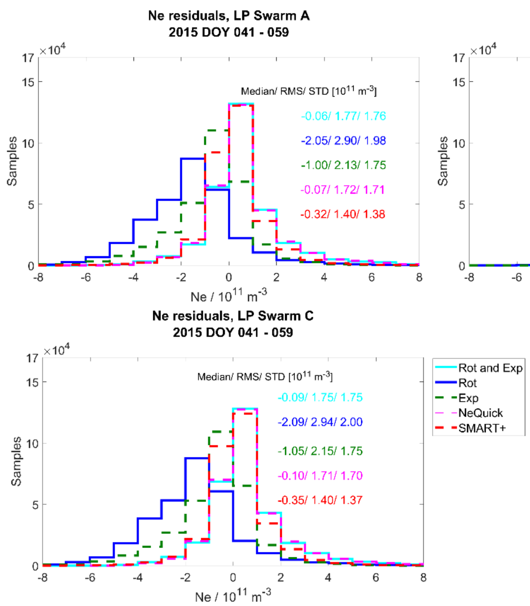

Figure 13: Validation with LP data – distribution of the Swarm A, B, C (separated) electron density residuals for the quiet period.

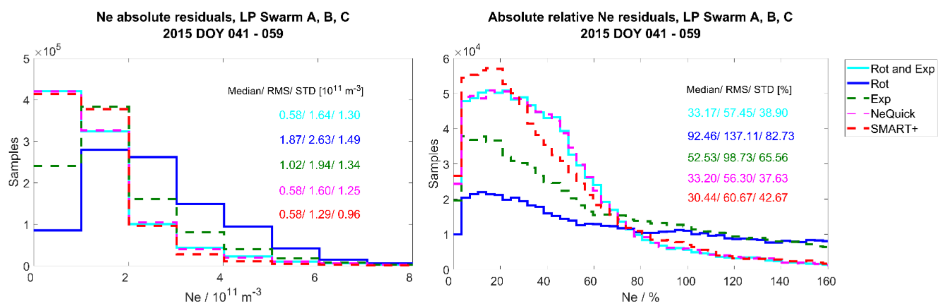

Figure 14: Validation with LP data – distribution of the Swarm absolute and absolute relative electron density residuals for the quiet period.

https://doi.org/10.5194/angeo-2020-39
Preprint. Discussion started: 23 June 2020

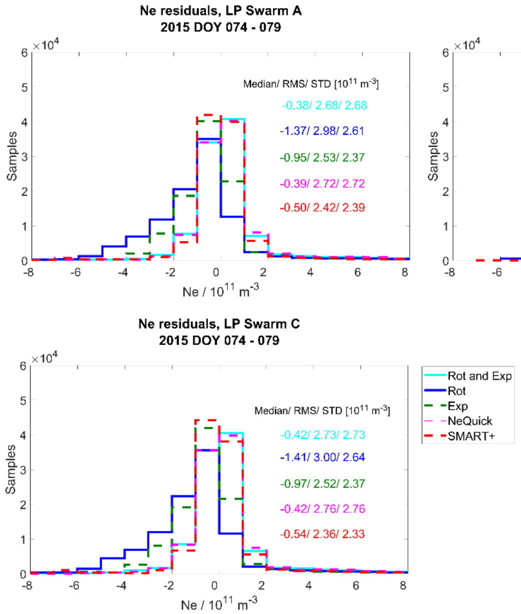

Figure 15: Validation with LP data – distribution of the Swarm A, B, C (separated) electron density residuals for the perturbed period.

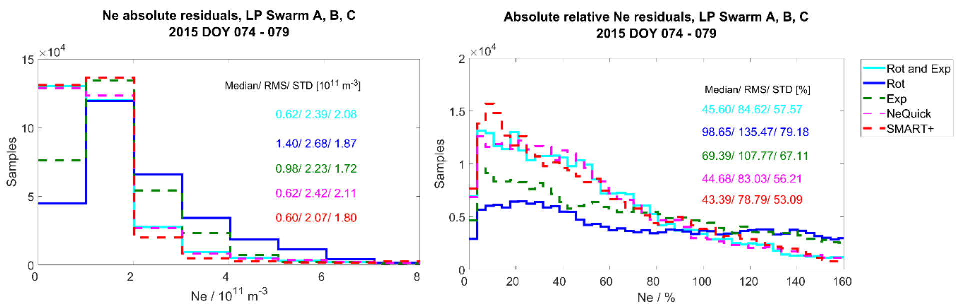

Figure 16: Validation with LP data – distribution of the Swarm absolute and absolute relative electron density residuals for the perturbed period.